

Gas diffusion in a pulmonary acinus model: experiments with hyperpolarized helium-3

Dayane Habib^{a,*}, Denis Grebenkov^{a,b}, Geneviève Guillot^a

^aU2R2M UMR8081 University Paris-Sud-CNRS, Bâtiment 220, 91405 Orsay Cedex, France

^bLPMC, CNRS-Ecole Polytechnique, F-91128 Palaiseau, France

Received 21 August 2007; revised 24 January 2008; accepted 24 February 2008

Abstract

Diffusion of hyperpolarized helium-3 in epoxy phantoms was experimentally studied by pulsed-gradient nuclear magnetic resonance (NMR). One phantom with a dichotomic branching structure densely filling a cubic volume was built using the Kitaoka algorithm to model a healthy human acinus. Two other phantoms, one with a different size and the other one with a partial destruction of the branched structure, were built to simulate changes occurring at the early stages of emphysema. Gas pressure and composition (mixture with nitrogen) were varied, thus exploring different diffusion regimes. Preliminary measurements in a cylindrical glass cell allowed us to calibrate the gradient intensity with 1% accuracy. Measurements of NMR signal attenuation due to gas diffusion were compared to a classical Gaussian model and to Monte Carlo simulations. In the slow diffusion regime, the Gaussian model was in reasonable agreement with experiments for low gradient intensity, but there was a significant systematic deviation at larger gradient intensity. An apparent diffusion coefficient D_{app} was deduced, and in agreement with previous findings, a linear decrease of D_{app}/D_0 with $D_0^{1/2}$ was observed, where D_0 is the free diffusion coefficient. In the regime of intermediate diffusion, experimental data could be described by the Gaussian model for very small gradient intensities only. The corresponding D_{app}/D_0 values seemed to reach a constant value. Monte Carlo simulations were generally in fair agreement with the measurements in both regimes. Our results suggest that, for diffusion times typical of medical magnetic resonance imaging, an increase in alveolar size has more impact on signal attenuation than a partial destruction of the branched structure at equivalent surface-to-volume ratio.

© 2008 Elsevier Inc. All rights reserved.

Keywords: Gas diffusion; Lung MRI; Hyperpolarized helium-3; Kitaoka model; Monte Carlo simulations

1. Introduction

Diffusion in porous media monitored by pulsed-field-gradient nuclear magnetic resonance (NMR) is known to be an efficient tool to probe their geometrical structure [1]. It has been used to investigate porous materials [2,3] as well as biological tissues [4,5] and has proven a remarkably rich diagnosis tool in medical magnetic resonance imaging (MRI) especially for brain studies [6,7]. Due to the large sensitivity gain provided with hyperpolarized (HP) gases (helium-3 or xenon-129), MRI can be used for lung ventilation imaging [8,9]. When combined with diffusion weighting, it is being

explored as a new modality for the diagnosis of emphysema [10,11]. The fact that pulmonary diseases are among the most widespread and represent a significant cause of mortality in the world [12] is a strong motivation for this promising application.

Lung airspaces are made up of a complex network with typically 23 levels of branching airways (for humans) that terminate in acinar gas exchange units, each of which is composed of hundreds of alveolar ducts lined with thousands of alveoli [13,14]. Most of the gas within the lung resides in the acini; their total number is estimated around $2.7 \cdot 10^4$ in a total lung volume of around 6 L, the volume of the elementary acinus being around 230 mm^3 , corresponding to a size of about 6 mm [15]. The size of alveolar ducts and alveolar sacs is estimated around 500 and 300 μm , respectively. Emphysema is defined as a disease of pulmonary tissue, which

* Corresponding author. Tel.: +33 0 1 69 15 41 34; fax: +33 0 1 69 15 41 36.
E-mail address: dayane_habib@yahoo.fr (D. Habib).

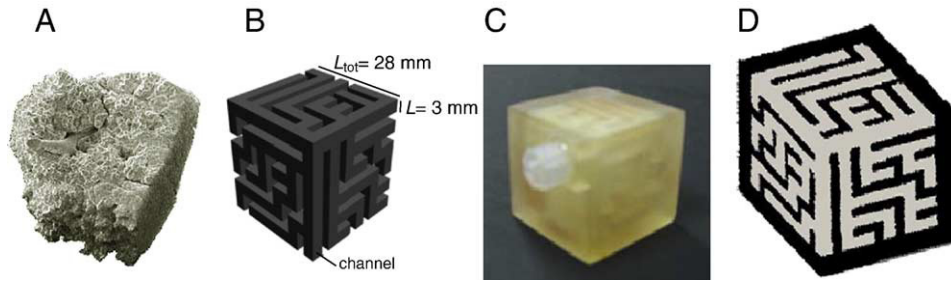


Fig. 1. Branched structure of the pulmonary acinus. (A) cast of a human acinus [13]. (B) branching geometry realization of a model acinus by the algorithm of Kitaoka used for the design of Phantom #1: what appears solid is the gas volume, and what appears transparent is the resin. (C) picture of Phantom #1 realized with epoxy resin. (D) 3D view of Phantom #1 geometry from X-ray CT.

results in partial destruction of the alveolar tissue and permanent enlargement of the airspaces distal to the terminal bronchioles, accompanied by destruction of their walls and without obvious fibrosis [16].

The possibility to diagnose emphysema by diffusion-weighted lung MRI with hyperpolarized helium-3 has been already investigated by several groups [10,11,17,18]. Indeed, within the timescale of diffusion encoding in diffusion-weighted MRI acquisitions (typically in the range of 1–10 ms), gas diffusion takes place over distances comparable to the size of several alveoli, given a free diffusion coefficient for helium in air of about $1 \text{ cm}^2/\text{s}$. Measurements of the apparent diffusion coefficient (ADC, which we will denote D_{app}) performed in healthy subjects and emphysematous patients, or on animal models, confirmed the expected trend of a larger ADC for emphysematous lungs. In these studies, a protocol with two values of b , $b=0$ and $b \neq 0$, was applied, the b value being determined by the specific gradient waveform (see Theory section). However, when more than two b -values were used, the signal attenuation was found to deviate from the expected behavior of an exponential decay on G^2 , G being the gradient intensity [19]. This observation revealed some ambiguity on the ADC quantification.

An anisotropic model was proposed by Yablonskiy et al. [19] to explain this behavior. The airways were described as cylinders randomly oriented in space and covered by alveolar sleeves, with gas motion along the axis of an airway less restricted than perpendicular to it. A theoretical relation for nonexponential NMR signal attenuation by diffusion was deduced and found in good agreement with experiments. In addition, airway radius and transverse diffusion coefficient were related, in view of providing a tool for early diagnosis of emphysema. Further numerical simulations were realized by Fichele et al. [20]. This anisotropic model supplies a simple analytical representation for NMR signal attenuation; moreover, it does not need any specific topological structure as an input.

Considering that the real acinus has a dichotomic branching structure, one could, however, question whether this fact influences NMR signal attenuation. This point was analyzed in a recent article by Grebenkov et al. [21], who suggested to take into account the branching morphology of

the acinus by using the algorithm of Kitaoka et al. [15]. The basic idea of the algorithm is to construct inside a cube a three-dimensional (3D) labyrinth which starts from an entrance, passes every point only once, and includes every branching. The acinus is thus modeled as a dichotomic structure with nonsymmetric branches of random lengths filling densely the volume of the cubic domain (Fig. 1). More exactly, this cubic domain represents only one subacinus (or 1/8 part of the acinus), which we will still call “acinus” in the rest of the text.

Tortuous channels of square cross-section profile (shown in Fig. 1B in dark gray) mimic alveolar ducts. These channels can be seen as connected small cubes, each of them representing an alveolar sac of eight alveoli, with a size of 0.3 mm in the original model of Kitaoka [15]. Moreover, the total alveolar surface area, the average length of the branches and the number of alveolar ducts, alveolar sacs and alveoli in the 3D acinar model are comparable to those of real acini. NMR signal attenuation due to gas diffusion in such acinus models was computed by Monte Carlo simulation [21]. Numerical results showed the importance of the branching structure on signal attenuation.

Experimental results of gas diffusion within lungs have also been reported with gases of diffusivity approximately 10 times lower than that of helium-3, such as hyperpolarized xenon (^{129}Xe) or fluorinated gases [22–24]. While Jacob et al. [24] reported an interesting sensitivity to emphysema from measurements with C_2F_6 in ex vivo healthy or emphysematous human lungs, Mata et al. [22] concluded from in vivo experiments in a rabbit model that a higher sensitivity to emphysema was observed with HP helium-3 rather than with ^{129}Xe .

This ensemble of results motivated us to perform experiments on models built with similar topological properties as those of real human acini. Phantoms with different sizes and connections were studied. One phantom considered as model of a healthy acinus had the smallest size and the connections between its unit cells were obtained from the algorithm of Kitaoka et al. [15]. For another phantom, some intercellular walls were removed in order to simulate the early stages of emphysema, thus considering early emphysema caused by the destruction of the internal

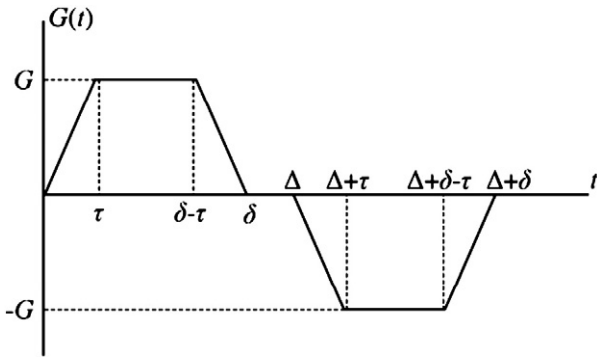


Fig. 2. Pulse gradient waveform used to sensitize the MR signal to helium-3 gas molecular diffusion. The parameters are the maximum gradient amplitude G , the diffusion time Δ , the pulse width δ , the pulse width δ and the ramp time τ .

walls of terminal bronchioles. The last phantom was built with the same connections as the “healthy” one, but with a somewhat larger size, to simulate the early stages of emphysema as due only to enlargement of the airspaces. A first motivation was to compare experimental results to Monte Carlo simulations, thus validating the simulation approach as an intermediate step for a better understanding of measurements on living lungs.

Moreover gas pressure and composition could be varied in our experiments, thus exploring different diffusion regimes and mimicking in vivo conditions accessible with different gases, depending on gas diffusivity. The detailed study of the dependence of signal attenuation on gradient intensity and on diffusion time is much easier to perform repeatedly on phantoms than in in vivo conditions. It should also give better guidelines in view of future protocols. Finally, the physical interpretation of diffusion weighted NMR data can be more clearly established by varying well-controlled parameters of the phantoms and examining the influence of these changes on signal attenuation.

2. Theory

Self-diffusion is the random translational motion of particles and is one of the fundamental forms of molecular transport. In the case of unrestricted self-diffusion in a homogeneous region, the mean square particle displacement along a given direction during time t is given by the expression:

$$\langle z^2 \rangle = 2D_0t \quad (1)$$

where D_0 is the free self-diffusion coefficient. The diffusive motion can be probed by NMR in Stejskal-Tanner pulsed field gradient experiment [25], in which a free induction decay (FID) signal is interrupted by two opposite-polarity gradient pulses, named the diffusion gradients (Fig. 2). In the presence of a bipolar diffusion gradient, nuclear spins gain a phase shift related to their displacement during the diffusion time. This phenomenon results in a decrease of the magnetic resonance

(MR) signal amplitude. In the case of unrestricted diffusion, the MR signal attenuation can be written as:

$$E = E_0 \exp(-b \cdot D_0) \quad (2)$$

In this formula, E_0 is the signal in the absence of diffusion-sensitizing gradient. The degree of diffusion sensitization is characterized by the b value, which, in turn, depends on the amplitude and timing of the gradient waveform. For a trapezoidal gradient waveform, the b value is given by [26]:

$$b = \gamma^2 G^2 \left[\delta^2 \left(\Delta - \frac{\delta}{3} \right) + \tau \left(\delta^2 - 2\Delta\delta + \Delta\tau - \frac{7}{6}\delta\tau + \frac{8}{15}\tau^2 \right) \right] \quad (3)$$

where γ is the gyromagnetic ratio of the observed nuclei, G , the maximum gradient amplitude; Δ , the diffusion time, δ , the pulse width and τ , the ramp time.

In the presence of confining walls or boundaries such as lung alveolar membranes, the motion of the nuclei is restricted, and the computation of the MR signal attenuation is a difficult task. Concerning the applications to lung MRI with HP gases, as well as in our own experimental study, the gas mean free path is always much smaller than the geometrical confinement. Therefore, the motion of the nuclei is still diffusive and exact solutions can be formally worked out in terms of infinite-dimension matrices, involving the Laplace operator eigenbasis [27–31]. For some simple geometries, such as the infinite slab or the infinite cylinder, the Laplace operator eigenbasis is known explicitly, and the numerical computation of the MR signal by means of the multiple correlation function approach [31] (or other matrix formalism) is rapid and very accurate. The MR signal can thus be found as a function of the three dimensionless variables p , q and h , built as ratios between different length (or time) scales. The first variable $p = D_0 2\Delta / L^2$ determines how far the nuclei travel with respect to the characteristic length L of the confinement (e.g., the radius of a cylinder). One can distinguish a slow diffusion regime ($p \ll 1$), in which only a small fraction of the nuclei is influenced by the restricting walls, from a regime of motional narrowing ($p \gg 1$), in which the nuclei explore the whole confining domain several times. The second variable $q = \gamma GL 2\Delta$ allows one to distinguish whether diffusion is probed at large or small length scales with respect to L . The third variable $h = L\rho / D_0$ quantifies the surface relaxation length D_0/ρ with respect to L , ρ being the surface relaxivity.

In complex porous media, exact solutions are not known, and the MR signal attenuation due to the bipolar gradient is often approximated by the equation:

$$E = E_0 \exp(-b \cdot D_{\text{app}}) \quad (4)$$

with the apparent diffusion coefficient D_{app} . The ADC increase observed in emphysematous lungs with respect to healthy ones was attributed to enlargement or/and partial

Table 1
Phantom parameters

Phantom name	L (cm)	L_{tot} (cm)	ν	S/V (cm $^{-1}$)
Phantom #1	0.30	2.80	100%	13.33
Phantom #2	0.30	2.80	83%	10.00
Phantom #3	0.40	3.73	100%	10.00

L , size of internal channel square section; L_{tot} , total internal size; ν , fraction of remaining internal walls; S/V , surface to volume ratio.

destruction of the alveolar tissue [10,17,19]. In spite of its numerous applications in different branches of NMR industry, this ADC notion remains limited to relatively small gradients of the magnetic field, when the Gaussian form of the macroscopic signal is still valid. Specific architecture or anisotropy of the morphology that confines diffusing nuclei makes the use of a single ADC questionable. Within the anisotropic diffusion model of Yablonskiy et al. [19] developed for the interpretation of lung MRI experiments with diffusion-weighting, the motion parallel and perpendicular to the cylinder axis can be characterized by a longitudinal (D_L) and a transverse (D_T) ADC, respectively. Both are related to the geometrical characteristics of the airway, e.g., D_T is proportional to the outer radii of a respiratory airway for a long enough diffusion time.

In the regime of slow diffusion, it has been shown that the apparent diffusion coefficient $D_{\text{app}}(t)$ decreases with time t and contains much information about the restrictions to diffusive motion. In particular, Mitra et al. [32,33] related the surface to volume ratio of a homogeneous isotropic porous medium to the asymptotic behavior of $D_{\text{app}}(t)$ at short times t . Their relation can be written in a general case as [31]:

$$\frac{D_{\text{app}}(t)}{D_0} \approx 1 - \frac{4}{3\sqrt{\pi}} \frac{\langle (t_2 - t_1)^{3/2} \rangle_2 S_e}{\langle (t_2 - t_1) \rangle_2 V} \sqrt{D_0 t} \quad (5)$$

where the dimensionless expression

$$\langle (t_2 - t_1)^\alpha \rangle_2 = \frac{1}{(2\Delta)^{2+\alpha}} \int_0^{2\Delta} dt_1 f(t_1) \int_{t_1}^{2\Delta} dt_2 f(t_2) (t_2 - t_1)^\alpha \quad (6)$$

(with $\alpha > 0$)

accounts for the effective gradient waveform $f(t)$ independently of its total duration $t=2\Delta$, and

$$S_e = \int_{\text{area}} d\text{s} \cos^2(\vec{e} \cdot \vec{n}(s)) \quad (7)$$

is the effective surface of the medium “exposed” to the applied gradient in a given direction \vec{e} [here $\vec{n}(s)$ is the unit vector perpendicular to the interface at point s]. Note that $S_e=S/d$ for homogeneous isotropic media, where d is the dimensionality of the system (here $d=3$), and S is the total surface area of the confining domain.

Relation (5) contains the first two terms of a series expansion in powers of \sqrt{t} . Higher power terms account for

corrections due to the curvature of the surfaces and surface relaxation [34]. This equation is valid when $(S_e/V)\sqrt{D_0 t} \ll 1$, a regime in which only a fraction of molecules (of order $(S_e/V)\sqrt{D_0 t}$) strikes the walls during time t , resulting in the linear decrease of $D_{\text{app}}(t)$ with \sqrt{t} . The slope of the linear decrease in \sqrt{t} is proportional to S_e/V , implying that an ADC measurement in this regime may allow the determination of S_e/V in the system. This relation has been verified experimentally with NMR of liquids imbibed in a variety of porous media [35–37].

3. Materials and methods

3.1. Phantom description

Phantoms were realized with a branching internal structure following the Kitaoka algorithm (Fig. 1) [15]. To obtain a reasonable accuracy on the phantom dimensions and sufficient signal, they were designed 10 times larger than the original model. Internal channels had a square section of size L and the total internal size was L_{tot} (Table 1). Phantom #1 was intended to represent a healthy acinus, and Phantoms #2 and #3 to represent early stages of emphysema. For Phantom #2, 17% of the internal walls of the original geometry were randomly removed; for Phantom #3, internal sizes were increased by 33%. In this way, it was chosen to highlight two different features of the early stages of emphysema: for Phantom #2, the removal of some internal walls (keeping the same size for the airway channels) represented a partial destruction of the terminal bronchiole walls, while for Phantom #3, the enlargement of the internal channel (keeping the same branching architecture as in the “healthy” acinus) corresponded to a permanent enlargement of distal airspaces. Note that the surface-to-volume ratio (S/V) was the same for Phantoms #2 and #3. The phantom geometry was described by a stereolithography (STL) file, which consisted of a list of triangles directed in space, giving a polyhedral representation of the object to be built. The phantoms were made by stereolithography from standard epoxy (Cresilas, Marcoussis, France), with an accuracy of ± 0.02 cm.

In order to check that the internal geometry of the phantoms had been correctly realized, they were examined by X-ray computed tomography (CT) on a clinical CT scan (Aquilion, Toshiba). 3D images were reconstructed with a pixel size of 0.299 mm in the Y and Z directions and for a slice thickness of 0.8 mm along the X direction. Fig. 1D shows a 3D-rendered view of the internal geometry of Phantom #1 from the CT scan acquisition.

A sealed glass cell filled with helium-3 at 16 hPa at room temperature was also used to adjust various experimental parameters such as NMR frequency, radiofrequency (RF) excitation, or gradient intensity, as described below. It was a cylinder of 4.5 ± 0.1 cm length and 4.5 ± 0.1 cm diameter. Room temperature was measured within 0.5°C , in order to minimize uncertainty on the free diffusion coefficient used as input for gradient calibration.

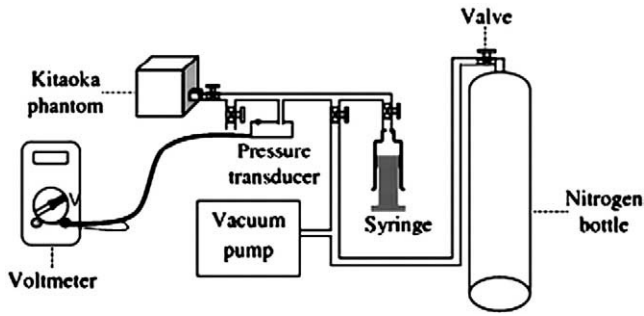


Fig. 3. Schematic assembly for measurements of the pressure P in the phantom: changing the valve positions, the phantom can be rinsed with nitrogen or evacuated; after rinsing, polarized helium is transferred into the phantom from the syringe; P is monitored with the pressure transducer and the voltmeter.

3.2. Gas production

Helium-3 was polarized by optical pumping (OP) using the technique of metastability exchange [38] in a 50 cm-long OP volume at a pressure of about 2 mbar, within a homogeneous magnetic field of 1.5 mT. A 2-W fiber laser at 1083 nm was used (Keopsys, Lannion, France). High-purity polarized helium-3 was allowed into the OP volume. The gas flow through the OP volume was controlled via the combination of a flow regulator and a peristaltic compressor [39]. The latter was used to extract the polarized gas from the OP cell and accumulate it into a storage glass cell at flow rates of around $2 \text{ cm}^3/\text{min}$ at standard pressure. For each experiment, about 0.5 to 10 cm^3 of helium-3, polarized up to 10% in the storage cell, was transferred back by the compressor into a syringe. For some experiments, nitrogen had been added into the storage cell prior to gas transfer in order to obtain mixtures (typically 65–70% nitrogen, 35–30% helium) with lower diffusion coefficients. The phantom was placed in the whole-body MR scanner prior to filling it with the hyperpolarized gas. Nitrogen or vacuum delivered

through a long 4-mm-inner-diameter tube, and the arrangement of different valves shown in Fig. 3 allowed us to evacuate the phantom or rinse it with nitrogen several times prior to filling it with hyperpolarized gas. The syringe filled with hyperpolarized gas was connected to the phantom immediately after its evacuation. The pressure transducer was of the type either 26PCCFA6D or XCA415AN (“Honeywell”, Gennevilliers, France); it was connected to the entry of the phantom to monitor its pressure during its evacuation and filling. The pressure in the phantom filled with the gas mixture was in the range 71 ± 15 – 2100 ± 52 hPa, and room temperature was controlled. The corresponding free diffusion coefficient D_0 , inversely proportional to the pressure P for a pure gas, can as well be computed for a gas mixture in a classical way [40]. It was in the range 28 – $0.43 \text{ cm}^2/\text{s}$, respectively.

3.3. Magnetic resonance acquisition

Helium-3 MR measurements were performed on a 0.1-T, whole-body MR scanner (Magnetech, France) controlled by an Apollo sequencer (Tecmag, Houston, TX, USA). A saddle-shaped RF coil was used for transmission with a loaded quality factor of about 45, and a 10-cm-diameter Helmholtz pair for reception with a loaded quality factor of about 340. Both coils were tuned at 3.29 MHz corresponding to the gyromagnetic ratio for helium-3 nuclei $\gamma \approx 2.04 \cdot 10^8 \text{ s}^{-1} \text{ T}^{-1}$. The MR sequence (Fig. 4) consisted of a series of 40 FIDs, collected during 256 ms with a bandwidth of $\pm 1 \text{ kHz}$, at the same delay of about 10 ms after a RF hard pulse of flip angle α adjusted around 15° . After every signal acquisition, an adequate crusher gradient pulse was applied on the three axes to destroy the remaining transverse magnetization. The repetition time was 282 ms. The first 10 FIDs were sampled after a bipolar gradient pulse of amplitude G ranging between 0 and 10 mT/m to obtain diffusion-weighted signals. This gradient had a trapezoidal

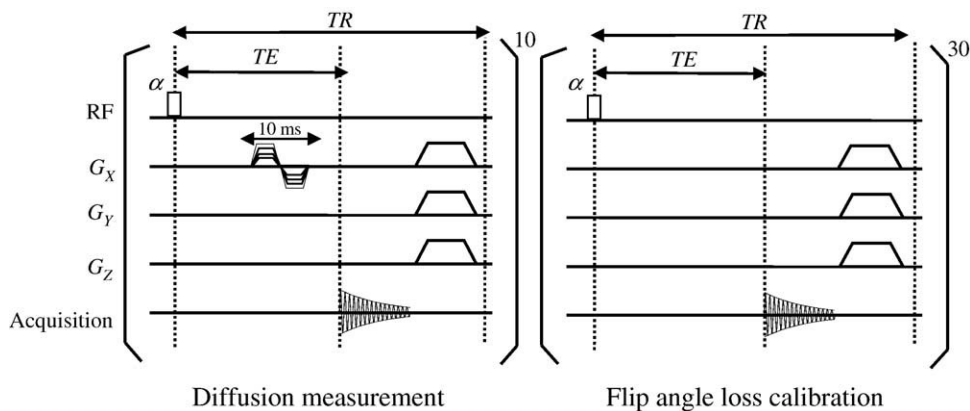


Fig. 4. Sequence of 40 FIDs, each collected during 256 ms at the same delay $TE=10$ ms after a RF hard pulse (flip angle α of about 15°) with a repetition time $TR=282$ ms. For the first 10 FIDs, a bipolar gradient pulse was applied. The last 30 FIDs were collected to calibrate flip angle loss and T_1 relaxation. A crusher gradient was applied on the three axes to destroy residual transverse magnetization. Experiments were performed independently to probe diffusion along each of the three axes.

shape (Fig. 2) of 10 ms total duration. The parameters of the diffusion-sensitizing gradient were: $\Delta = \delta = 5$ ms and the rise and fall times $\tau = 2.2$ ms. The factor $\frac{((t_2 - t_1)^{3/2})_2}{((t_2 - t_1)_2)}$ in Eq. (5) was then equal to 0.8281, using Eq. (6) for computing it numerically. The last 30 FIDs were sampled to accurately determine signal loss by RF depolarization and T_1 relaxation. Diffusion weighting was measured on each of the three axes x , y and z in separate experiments. Identical power was applied for all RF pulses with a duration of 150 μ s ($B_1 \approx 8.55$ μ T). The same sequence was used for the sealed cell, with a diffusion gradient 10 times smaller.

Measurements with the cylindrical glass cell were performed to adjust finely the gradient offsets and the gradient intensity on the three axes. The sequencer controlled the gradient offset and intensity with an accuracy of 1.95 μ T/m. Shimming was performed by adjusting the gradient offset on the three axes to get the longest possible FID in the glass cell. No other shimming was possible. The gradient intensity was adjusted by comparing the measured attenuation to its theoretical prediction (see Theory, Results and Discussion sections).

3.4. Data analysis

3.4.1. FID initial magnitude

Each FID initial magnitude was determined by fitting the FID decay complex data using routines from Matlab (Mathworks, Sèvres, France). The FID shape was neither exponential nor Gaussian, but phenomenologically, it could be fitted as a product of both in order to keep a minimal number of parameters:

$$E(t) = E_0 \exp\left(-\frac{t}{T_2}\right) \exp\left(-\frac{t^2}{2\sigma^2}\right) \exp(i(2\pi\nu t + \phi)) \quad (8)$$

In this equation, $E(t)$ is the complex FID signal, E_0 , the initial FID magnitude, T_2 , the time constant, σ , the Gaussian half width ν , the frequency and ϕ , the phase.

In a given experiment, the FID had always more or less the same shape, so the four adjustable parameters (T_2 , σ , ν and ϕ) were computed only for data of strong enough signal-to-noise ratio, typically higher than 100, and were used for the other excitations. The signal-to-noise ratio was defined as E_0 divided by the noise N (standard deviation of the real part for the last 100 FID points). The accuracy on E_0 was determined by fitting artificial data, computed from Eq. (8) with the addition of random Gaussian noise, and for values of the FID magnitude and of the FID shape parameters typical of experimental data. The noise amplitude N was multiplied by random numbers normally distributed with zero mean and standard deviation 1. This analysis was repeated 10 times and from the resulting fitted magnitudes the average amplitude value and the corresponding standard deviation were found. The FID initial magnitude E_0 was thus determined with an accuracy better than 0.08% for pressures higher than 180 hPa and better than 0.16% for smaller pressures.

3.4.2. Effective flip angle

Between each RF excitation, the longitudinal magnetization decays due to both RF loss per excitation and longitudinal relaxation during the repetition time. For a series of RF pulses all applied with the same low flip angle α_{real} , their combined effects result in a fractional loss of signal amplitude from one excitation to the next by $\cos(\alpha)$, where α is an effective flip angle somewhat larger than α_{real} . To evaluate α , the amplitude of the last 30 FIDs were fitted to an exponential decay $\exp(-n\beta)$, where n is the FID index (1–30) and $\alpha = \arccos[\exp(-\beta)]$. It was not necessary to assess independently the longitudinal relaxation, which contributed only by a minor amount to the effective decay. For all measurements, α was determined with an accuracy better than 0.07%, which was found in the same way as the accuracy on the FID initial magnitude.

3.4.3. Data normalization

Once the flip angle was accurately determined, the contribution to signal attenuation from the diffusion gradient (first 10 FIDs) was computed by eliminating the contribution due to RF pulse repetition (including T_1 relaxation). The data were normalized to the first FID magnitude. The normalized signal $E_{\text{norm}}(n)$ for the n th FID was computed from Eq. (9):

$$E_{\text{norm}}(n) = \frac{E(n)}{E(1)[\cos(\alpha)]^{(n-1)}} \quad (9)$$

where $E(n)$ is the initial magnitude of the n th FID.

The error on E_{norm} was computed as:

$$\frac{dE_{\text{norm}}(n)}{E_{\text{norm}}(n)} = \left[\frac{dE(n)}{E(n)} + \frac{dE(1)}{E(1)} + (n-1)tg(\alpha)d\alpha \right] \quad (10)$$

where $d\alpha$ is the absolute error on α .

$E_{\text{norm}}(n)$ was determined with an accuracy better than 0.1% for pressures above 180 hPa, and better than 0.17% for lower pressures.

3.5. Numerical calculations and Monte Carlo simulations

The signal attenuation in the sealed glass cell was computed using the multiple correlation function library developed by one of the authors [41].

Monte Carlo simulations were used to compute signal attenuation due to gas diffusion in the Kitaoka phantom as described in detail in [21]. The diffusion coefficient D_0 , as determined from the experimental conditions of each measurement, the gyromagnetic ratio γ , the profile $f(t)$ of the magnetic field gradient and its duration were fixed. The reflected Brownian motion trajectory was modeled as a sequence of m random jumps started from a randomly chosen point inside the phantom. For each jump, the displacements Δx , Δy and Δz along the three spatial axes were independent and normally distributed, their variances $\langle \Delta x^2 \rangle$, $\langle \Delta y^2 \rangle$ and $\langle \Delta z^2 \rangle$ being equal to $(2D_0 \Delta t/m)$. The number m of jumps for the 10 ms gradient duration was set to 1000 and checked to be sufficiently large to model a Brownian trajectory. The simulation of a

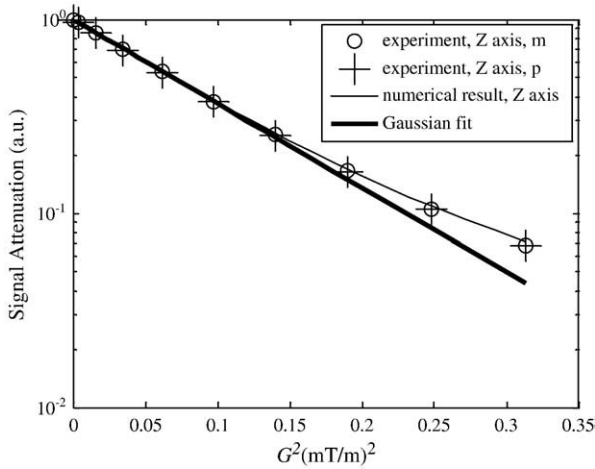


Fig. 5. Gradient calibration: experimental signal attenuation in the glass cell as a function of the applied diffusion gradient for polarity m and p (symbols), and numerical result (lines) for the Z gradient direction. The good accuracy on signal amplitude (better than 0.1–0.17%) corresponded to a 1% accuracy of gradient intensity (see text for other sources of uncertainty). Note the deviation to the Gaussian fit, visible even in this simple geometry at a p value of 0.06.

single Brownian trajectory was repeated N times, to record the phase ϕ_k accumulated along this k th trajectory:

$$\phi_k = \gamma G \left[\sum_{j=1}^{m/2} f_j X_j - \sum_{j=m/2+1}^m f_j X_j \right] \quad (11)$$

X_j being the projection of the trajectory at step j onto the direction of the applied gradient, f_j representing the effective gradient waveform $f(t)$ with discrete time steps.

The NMR signal E as a function of the gradient amplitude was computed as the average over all trajectories of the individual spin magnetizations $\exp(i\phi_k)$:

$$E = \frac{1}{N} \sum_{k=1}^N e^{i\phi_k} \quad (12)$$

The choice of N equal to one million provided an accuracy of order of 10^{-3} on the NMR signal attenuation that was sufficient for comparison to experimental data. In contrast with [21,42], where an arbitrary acinus orientation in the chest was taken into account by averaging over all possible gradient directions in 3D space, in the present work the computation was done for a fixed orientation of the phantom in the scanner with respect to the three gradient directions.

4. Results

4.1. Gradient offset adjustment and gradient intensity calibration

The gradient offsets were adjusted and the gradient intensity was calibrated from measurements performed with the sealed glass cell at 16 hPa.

The gradient offsets could be finely adjusted by searching the values giving the slowest FID decay in the glass cell. They were determined on the three axes with an accuracy of $\pm 1.95 \mu\text{T/m}$.

After gradient offset adjustment, the gradient intensity was calibrated by comparison of experimental signal attenuation due to diffusion in the glass cell to simulated data, using the free diffusion coefficient of the gas as input for the simulation. Fig. 5 shows signal attenuation as a function of the diffusion-sensitizing gradient G applied along the z gradient axis. Data are presented for the two polarities of the applied bipolar diffusion-sensitizing gradient G , either m (negative then positive) or p (positive then negative). Experimental results for both polarities were coincident, except for the x -axis, for which a 4% deviation was observed. Note that signal attenuation at this low pressure already significantly deviated from a simple Gaussian behavior, although the cell dimensions and the gas free diffusion coefficient ($D_0=123.93 \text{ cm}^2/\text{s}$) would imply a slow-diffusion regime ($p=0.06$). The gradient intensity was adjusted to obtain the best possible agreement to numerical results computed from the multiple correlation function approach [31]. It was then calibrated within 1%, considering the uncertainty on exact dimensions and pressure in the glass cell. The latter were the main sources of error, considering the good accuracy on signal attenuation (0.1–0.17% as discussed above).

4.2. Experiments with phantoms

Fig. 6 shows the normalized signal attenuation as a function of the applied diffusion-sensitizing gradient G for both experimental and numerical results at different pressures in Phantom #1. The corresponding p values were, respectively, equal to 0.3, 0.63, 1.06 and 1.68 when P was respectively equal to 732, 345, 206 and 130 hPa. Results are shown only for the diffusion gradient applied along the x -axis, and similar results were obtained when the diffusion gradient was applied along axes y and z . Error bars were smaller than the symbol size and are not shown. The signal attenuation for the Gaussian model is also presented for all pressures. Due to significant deviations from this simple model (as seen in Fig. 6), it was chosen to assess the apparent diffusion coefficient in the following way: only the data points for low G that gave a fit error smaller than the estimated noise level were taken into account, typically 2–5 points. The limiting G value up to which fit was acceptable appeared weaker and weaker as pressure was decreased (Fig. 6A–D). The numerical results were in better agreement with the experimental results. Only at low pressures (Fig. 6D) and for G higher than 2.5 mT/m, numerical results were systematically found above experimental data. One can also note changes in the shape of the decay curve when the pressure was lowered: the initial decay for $G < 2$ mT/m appeared faster and faster; moreover for higher G the decay showed increasingly stronger deviation from the Gaussian behavior.

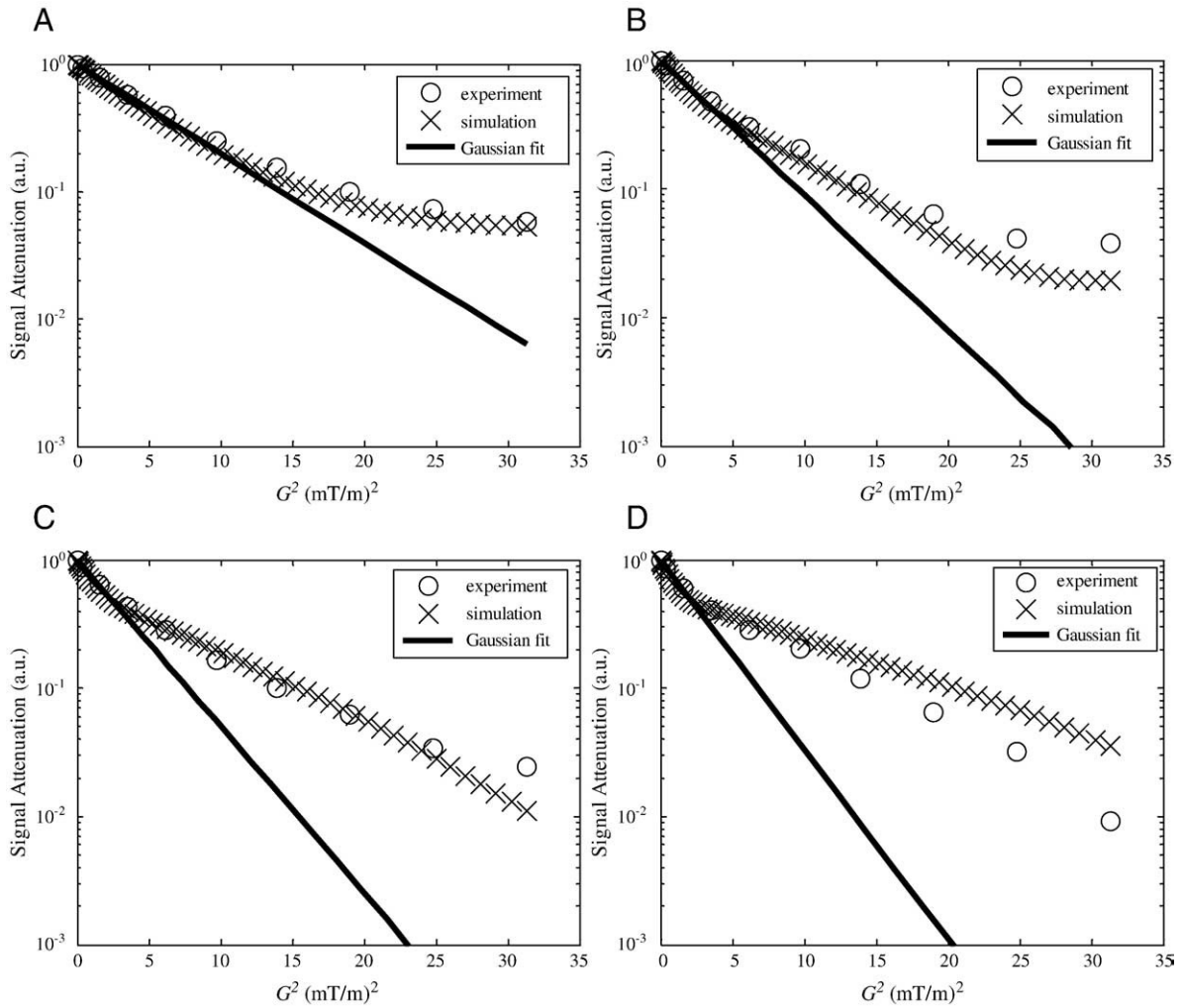


Fig. 6. Signal attenuation in Phantom #1 as a function of the diffusion sensitizing gradient G applied along the x -axis for different pressures P in the phantom: $P=732$ hPa ($p=0.30$) (A), $P=345$ hPa ($p=0.63$) (B), $P=206$ hPa ($p=1.06$) (C) and $P=130$ hPa ($p=1.68$) (D). Experimental data (o) are compared to numerical simulation results (\times) and to a Gaussian fit (line). Error bars were smaller than the symbol size and are not shown. The corresponding values of D and to a Gaussian fit (line). Error bars were smaller than the symbol size and are not shown. The corresponding values of D_{app} and D_0 are presented in Table 2.

Fig. 7 shows the normalized signal attenuation as a function of the diffusion-sensitizing gradient G applied along each of the three axes x , y and z at similar pressures (corresponding to p around 1.6) in Phantom #1. Gaussian fits are also shown. Experimental data points were almost coincident for data acquired with the X and Y gradients. Since the Gaussian fit gave an identical result for both axes x and y , it is only shown for the x -axis. On the other hand, for the z -axis and at a slightly higher pressure, experimental points were above those from the two other gradient axes but approached comparable value for $G > 3.5$ mT/m. As already seen in Fig. 6, the Gaussian fit was in agreement with the experiments only for weak gradients $G \leq 1.2$ mT/m. For higher G and for all axes, the Gaussian fit was systematically below the experimental data.

Fig. 8 shows the signal attenuation as a function of the diffusion sensitizing-gradient applied along the x -axis for the three phantoms at similar pressures: one series was acquired

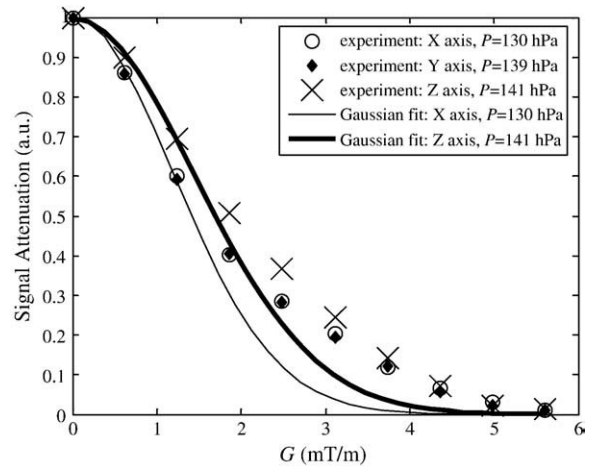


Fig. 7. Signal attenuation in Phantom #1 for the diffusion sensitizing gradient G applied separately along the three axes x , y and z for similar pressures. Experimental data (symbols) and corresponding Gaussian fits (lines).

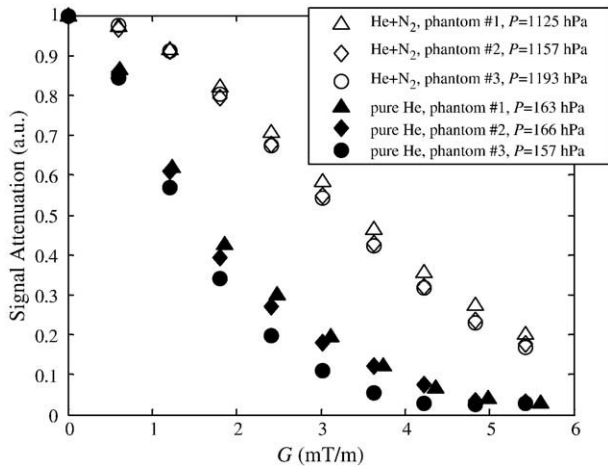


Fig. 8. Signal attenuation in the three phantoms as a function of the diffusion sensitizing gradient G along the x -axis and for similar pressures. Two series of data are shown, one was acquired for helium in nitrogen at $P=1158\pm34$ hPa and the other one for pure helium at $P=162\pm26$ hPa.

with a mixture of helium in nitrogen for pressures ranging between 1125 and 1193 hPa (with p around .09), and the other with pure helium for pressures ranging between 157 and 166 hPa (and p around 1.3). At the higher pressures, experimental data were coincident for Phantoms #2 and #3, about 4% below those of Phantom #1. At the lower pressures, Phantom #3 presented the strongest signal attenuation, and Phantom #1, the lowest.

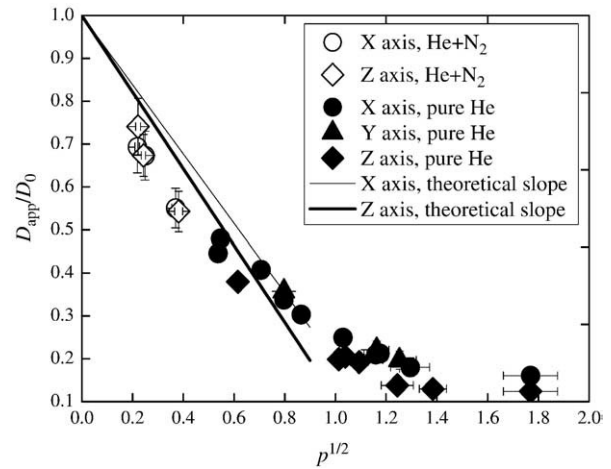


Fig. 9. Apparent diffusion coefficient D_{app} for the experiments conducted on Phantom #1, deduced from a fit of Eq. (4) to experimental signal attenuation in the low G limit (see text): D_{app}/D_0 is plotted versus $D_0^{-1/2}$ for pure He (full symbols) and for He in N_2 (empty symbols), for experiments with the diffusion sensitizing gradient along x , y or z . The full lines show the theoretical slopes expected for axes x and z , computed from Eq. (5).

Table 2 shows the free diffusion coefficients D_0 at given pressure P and temperature T and the resulting D_{app} values for the experiments performed along each gradient axis in Phantom #1. The D_0 values were computed as detailed in Appendix B of Ref. [40]. The relatively large error on D_0 for experiments performed with helium-nitrogen mixtures was due to the poor accuracy of the pressure transducer at the

Table 2
 D_{app} and D_0 values for Phantom #1

Gas composition	Gradient axis	T (K)	P (hPa)	D_0 (cm ² /s)	D_{app} (cm ² /s)
He+N ₂	x	295.8±0.6	2100±52	0.43±0.07	0.2980±0.0006
He+N ₂	x	295.8±0.6	1609±43	0.56±0.09	0.3770±0.0008
He+N ₂	x	296.4±0.6	717±27	1.23±0.2	0.677±0.001
He+N ₂	z	296.1±0.6	1965±50	0.440±0.075	0.326±0.002
He+N ₂	z	295.8±0.6	1698±45	0.53±0.074	0.357±0.001
He+N ₂	z	296.4±0.6	672±26	1.31±0.22	0.711±0.002
He	x	296.5±0.1	762±28	2.60±0.10	1.160±0.003
He	x	295.1±0.5	732±12	2.69±0.05	1.292±0.006
He	x	295.1±0.5	438±12	4.49±0.13	1.83±0.02
He	x	295.1±0.5	345±14	5.71±0.24	1.93±0.01
He	x	295.1±0.5	292±16	6.7±0.4	2.04±0.02
He	x	295.1±0.5	206±21	9.5±0.9	2.38±0.02
He	x	295.1±0.5	163±26	12±1.9	2.54±0.06
He	x	296.5±0.1	160±17	12.4±1.44	2.64±0.06
He	x	295.1±0.5	130±31	15.1±3.57	2.72±0.03
He	x	296.5±0.1	71±15	28±6.8	4.52±0.06
He	y	295.1±0.5	345±14	5.71±0.24	2.04±0.01
He	y	295.1±0.5	162±26	12±1.97	2.69±0.04
He	y	295.1±0.5	139±29	14.1±2.97	2.78±0.02
He	z	296.5±0.1	583±25	3.40±0.15	1.290±0.006
He	z	295.1±0.5	213±20	9.3±0.91	1.84±0.02
He	z	296.5±0.1	204±18	9.7±0.92	1.99±0.05
He	z	295.1±0.5	183±23	10.76±1.39	2.07±0.08
He	z	295.1±0.5	141±29	13.92±2.85	1.92±0.02
He	z	296.5±0.1	115±16	17.2±2.7	2.23±0.03
He	z	296.5±0.1	71±15	28±6.8	3.49±0.07

storage cell that caused a 13% uncertainty on the helium partial pressure. When P increased, D_{app} generally decreased, similarly to D_0 , but slower. Fig. 9 shows D_{app}/D_0 versus $p^{1/2}$ for all data reported in Table 2. All data were collected for the same diffusion gradient timing, but decreasing P was equivalent to increasing D_0 and, thus, p . The observed behavior for data collected at the highest pressures (i.e., $p < 5$) corresponded to the linear decrease of D_{app}/D_0 versus $D_0^{1/2}$ predicted by Mitra et al. [32] and de Swiet et al. [34] and already observed in different porous systems [35,37]. Then for p higher than about 1, the data tended to level off to a constant value depending on the gradient direction.

5. Discussion

Our experimental study with a model acinus system was undertaken in order to better understand NMR signal attenuation by diffusion in human lungs. With a model system, it was possible to obtain accurate predictions from numerical simulation. The experimental measurements then confirmed its validity. Moreover, the pressure in the phantoms could be changed in a relatively large range, thus simulating systems with different effective diffusion length scales. Indeed, decreasing the pressure is equivalent to increasing D_0 , that is, the mean free path of helium-3 atoms in the phantom. The mean free path stayed much smaller than the channel size. Therefore, the physical mechanisms governing signal attenuation by diffusion remained the same over the whole range of pressures. Changing the pressure allowed us to control the restriction to gas diffusion: the characteristic parameter p was varied in the range $p=0.047$ – 3.11 . The intensity of the gradient and its time profile corresponded to q in the range 0 – 61.2 . Here, p and q were computed taking for L the internal channel size of Phantom #1 (Table 1). Note that there were, in fact, two length scales in the phantoms (L and L_{tot}), differing by about one order of magnitude. The lengths explored by diffusion during the bipolar gradient pulse at the minimal and maximal pressures reported in Table 2 were thus, respectively, 0.53 and 0.06 cm, as compared to the channel size of 0.3 cm in Phantom #1.

The changing shapes of the signal attenuation with the gradient intensity for different pressures and gas compositions can then be related to the transition between regimes of slow diffusion ($p < 0.1$) and of intermediate diffusion ($p > 1$). At high pressures (or low D_0), the restriction is mainly due to the basic cell of our phantoms (more or less a 0.3 -cm slab in two spatial directions). At lower pressures (or higher D_0), the nuclei explore a longer length than the basic cell of the phantoms so that their branching geometry is expected to play a role. For in vivo MRI studies of the lung with helium-3, typical values correspond to those of the intermediate regime.

The detailed study of the influence on signal attenuation of internal geometrical details and topology has been already undertaken [21] in a Kitaoka phantom at its original scale,

closer to the human lung. This numerical study has shown in particular that destruction of the alveolar tissue by creating loops in the branched structure (thus simulating changes expected to occur in early stages of emphysema) caused faster diffusion and stronger signal attenuation than removal of septum membranes, with equivalent changes in surface to volume ratio. Differences in topology of the channels at the same surface-to-volume ratio could be distinguished, but only at long-enough diffusion times.

From the available signal to noise ratio of the collected FIDs, typically higher than 100, the protocol used to analyze the data gave us an excellent accuracy on signal attenuation, typically in the range between 0.1% and 0.17% . This improvement can be mainly attributed to the large number of points measured on each FID, which increased the accuracy on initial signal amplitude. This opened the possibility of making accurate comparison to numerical simulations.

First, we addressed the problem of gradient calibration and gradient offset adjustment. The offset could be adjusted within $1.95 \mu\text{T/m}$; this value was ultimately limited by the digitized signal controlling gradient offsets. The gradient intensity could be calibrated with a 1% accuracy by comparison of experiments to numerical results, the main source of error being the accuracy at which the cell dimensions and the pressure of helium-3 inside it were known. In a former experiment, the gradient amplitude had been calibrated by HP helium-3 T_2 measurement in a syringe at room pressure and temperature, which were both accurately determined [43]. Comparing the two calibration procedures, the deviation was of 1% on the x -axis, and of 2.9% on the two other axes. This is better than the estimated 4% accuracy of the former method, which was mainly due to T_2 fit uncertainty. From these results, the gradient intensities applied in our experiments with the acinus phantoms were known with an accuracy of 1% .

The measurements of signal attenuation due to diffusion in the acinus phantoms, when plotted as a function of the gradient intensity G , deviated from a Gaussian behavior, with an attenuation systematically above the Gaussian small- G limit. Nevertheless the Gaussian behavior at small G enabled us to compute D_{app} for different pressures and along the three spatial directions. The reduced diffusivity D_{app}/D_0 was relatively consistent with an initial linear decrease when plotted against $p^{1/2}$ (Fig. 9). The slope was expected to differ along each spatial direction. Indeed, the surfaces at the origin of restricted diffusion were somewhat different along each direction: the expected values computed from Eq. (7) are $S_x/V=4.32 \text{ cm}^{-1}$, $S_y/V=4.25 \text{ cm}^{-1}$, $S_z/V=4.78 \text{ cm}^{-1}$ for Phantom #1. However, the 16% uncertainty on D_0 for the experiments with helium–nitrogen mixtures did not allow us to confirm this sample anisotropy. For $p > 1$, D_{app}/D_0 approached a constant. This indeed corresponds to low enough pressures for which $\sqrt{D_0\Delta}$ becomes larger than the internal channel size in the phantom.

The deviation from the Gaussian behavior occurred above a gradient value (or q value) depending on pressure, and

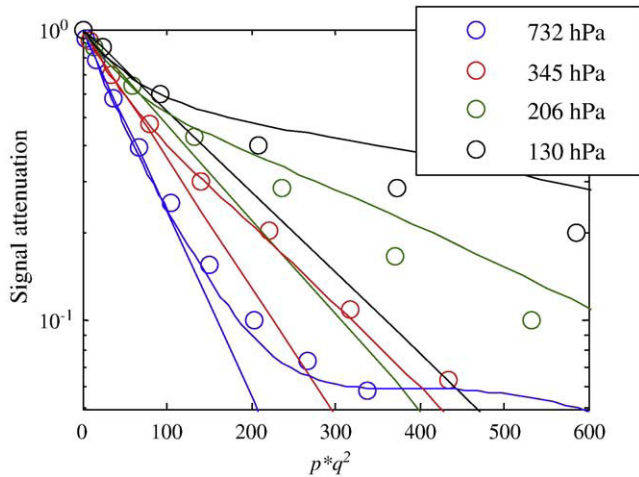


Fig. 10. Experimental signal attenuation in Phantom #1 for different pressures: same data as in Fig. 6, but all in the same plot, and along the dimensionless variable $p q^2$. Experimental data are shown as symbols, full lines represent the respective Gaussian fits and dashed lines, the numerical results. Note that the scale has been intentionally limited to better observe the deviation to the Gaussian fit, which occurs for all data shown for $p q^2$ around 100.

varying the pressure P inside the phantom changed the shape of the signal attenuation plotted versus G . Indeed, the deviation from the Gaussian behavior at large G , which was already visible at the higher P values, was strongly enhanced and appeared at smaller G values when P was decreased (Fig. 6). This change of shape found in the experiments was as well predicted from the numerical simulations.

The changes of signal attenuation shape with pressure in the phantom should nevertheless follow a general behavior related to the dimensionless parameters p and q . At least, that can be theoretically expected in the small- p limit, where all curves to first order follow a Gaussian behavior. Fig. 10 shows the same experimental data as those of Fig. 6 but plotted against the dimensionless variable $p q^2$. Since for each pressure the restriction to diffusion D_{app}/D_0 changed, it is not surprising that the initial slope of the curves changed as well. Note that the low-pressure data now presented the fastest decay with $p q^2$, due to the fact that they also correspond to the lowest restriction to diffusion. However, on the other hand, the restricted range shown on Fig. 10 better gives evidence that in this representation, all experimental data show a departure from the Gaussian behavior for $p q^2$ around 100. A similar observation could be made as well for the data acquired with the two other phantoms, independently of their geometrical details. An important general conclusion to that observation is that the limiting q value q_{limit} for which the signal attenuation deviates from a Gaussian, can be related to the p value of the corresponding experiment by: $q_{limit} \approx 10/p^{1/2}$. A G value G_{lim} can be easily computed, in agreement with our observations on Figs. 6–8. Although this relation for q_{limit} should depend on the sequence (particularly gradient waveform and timing), this conclusion may help to predict

the range of G values to be used in in vivo MRI, for a more reliable and quantitative assessment of ADC values.

By contrast, the numerical simulations correctly predicted the experimental measurements over the whole gradient range and for all pressures. A discrepancy between simulation and experiments for the data collected at the lowest pressures (See Fig. 6D) remained. At first sight, a potential source for this deviation might be attributed to surface relaxation that was not initially considered in the numerical simulations. But since gas diffusion is quite rapid in this case, the normalization protocol used for the experimental data should eliminate relaxation effects, in agreement with few numerical simulations taking into account surface relaxation. Susceptibility-induced gradients would also cause similar effects but, again, should be eliminated by data normalization. Another possible explanation could be geometrical imperfections of the phantoms with respect to their design. The pixel size of the CT scan data was sufficient to check that, for the three phantoms, the branching geometry had been correctly realized and that their dimensions were in the correct ratio, but not to evaluate details such as surface roughness or other minor defects.

Comparing data acquired at similar pressures in the three phantoms (Fig. 8), Phantoms #2 and #3 gave comparable experimental signal attenuation in the slow diffusion regime (helium–nitrogen mixture at the higher pressures, corresponding to p around 0.09), as expected, since they were built with identical S/V . Indeed, in this regime, signal attenuation mostly shows a Gaussian behavior, with D_{app} linearly related to S/V . By contrast, in the intermediate regime (pure helium, with p around 1.3), increasing the internal channel size by 33% had a stronger effect on signal attenuation than destroying 17% of the internal walls. This observation is complementary to previous simulation results [21], which showed that the destruction of septum membranes, which was done keeping a constant channel size, had a much weaker impact on restricted diffusion and the consequent signal attenuation than a partial destruction of the acinus branched structure.

It is somewhat interesting to tentatively compute ADC values following a similar method as in in vivo experiments, that is, using only two b values, $b=0$ and, for example, one giving a signal attenuation of about 0.5, from the data obtained in Phantoms #2 and #3 in the intermediate regime. We have to stress here that these measurements were obtained with $p=1.3$, that is, relatively comparable to conditions of in vivo acquisitions with shorter diffusion times (1.6 ms), but in real lungs, that is, with smaller airways. From the signal attenuation obtained at $G=1.8$ mT/m corresponding to a relatively moderate b value of about 0.4 s/cm², the corresponding ADC values would be 2.4 cm²/s (Phantom #2) and 2.8 cm²/s (Phantom #3), although Phantoms #2 and #3 have been built with identical S/V . Taking the signal attenuation obtained with $G=3$ mT/m (b around 1 s/cm²), these values would be reduced to 1.6 cm²/s (Phantom #2) and 2.3 cm²/s (Phantom #3). Note that

the measurements performed in the slow diffusion regime correctly confirmed that the two phantoms had indeed identical S/V . This observation can be also related to the study of Woods et al. [18], who found a strong correlation between S/V assessed by histology and helium-3 ADC measured in an intermediate diffusion regime in healthy and emphysematous ex vivo lungs.

6. Conclusion

Restricted diffusion of hyperpolarized helium-3 was studied both experimentally and numerically in model pulmonary acini, changing the pressure on a large range, thus systematically exploring transition between regimes of slow and intermediate diffusion: the parameter p was varied in the range 0.047–3.11.

In the slow diffusion regime ($p < 1$, corresponding to higher pressures), the Gaussian model was in reasonable agreement with experimentally observed signal attenuation for low gradient intensity, but there was a systematic deviation at larger gradient intensity. The q value above which this deviation became significant appeared to decrease as p increased and followed a $p^{-1/2}$ scaling law. As in similar studies with porous media, we observed that the restriction to diffusion corresponded to a linear decrease of D_{app}/D_0 with $p^{1/2}$.

In conditions of intermediate diffusion ($p > 1$, corresponding to lower pressures), experimental data could be described by the Gaussian model for small gradient intensities only. Moreover the corresponding D_{app}/D_0 seemed to reach a constant value. The deviation between the Gaussian model prediction and the data (of order 20%) was much larger than experimental uncertainty.

Numerical data were generally in fair agreement with our measurements on the whole pressure range, within the experimental uncertainty (better than 0.2%). But there was a deviation for the lower pressures, numerical results being systematically above experimental data at the larger gradients by a few percent. This remaining discrepancy was tentatively attributed to geometrical defects of the phantoms.

Some more general conclusions can be drawn from our study, in view of a better understanding of diffusion-weighted lung MRI data with different gases. Indeed, using the same bipolar pulse duration as in our study in real lungs, and with helium-3 diluted in air (D_0 is then about 1 cm²/s), the length explored by free diffusion would be about 0.1 cm, that is, two or three times larger than the size estimated for alveolar sacs or ducts. With a fluorinated gas such as C₂F₆ (D_0 is 0.03 cm²/s from Jacob et al. [24]), this would be only 0.017 cm. Depending on the pulse duration used, p is therefore typically in the range 1–10 with helium-3 in human lungs, whereas it is in the range 0.01–0.1 with C₂F₆. In the intermediate diffusion regime ($p > 1$), one should not expect that the ADC value is simply related to the surface to volume ratio of the lung. Great care should be taken when comparing data from different sources acquired with different

b values and timings, due to the severe insufficiency of the Gaussian model in the intermediate diffusion regime. Moreover, it may be strongly misleading to compute an ADC from only two b values, except if very small gradient intensities are used (but at the cost of a lower diffusion contrast, and thus of a poorer accuracy). By contrast with C₂F₆, a more direct access to S/V changes should be obtained, although the slow diffusion of this gas could be problematic for establishing reproducible experimental conditions [24].

Our results suggest that an increase in alveolar size has more impact on signal attenuation than a partial destruction of the branched structure. However, the diffusion time in this work was relatively short and gas atoms travelled at most distances of a few internal channels. When performing measurements at longer times to insure that gas truly explore the acinus branched structure, this conclusion could be reconsidered. It has been recently shown that longer time scales are experimentally accessible, using sequences based on stimulated or multiple echoes [44,45]. A several-fold decrease of ADC when the diffusion time varied from millisecond to seconds was observed in humans [44]. Another approach using magnetization tagging has also been successfully shown to give access to long-range diffusion [46]. These techniques should open a way to assess diffusion over sizes comparable to or larger than the acinus and thus appear promising for a more efficient detection of emphysema.

Acknowledgments

The authors are grateful to Ludovic de Rochefort for his contribution in designing the STL files, to Emmanuel Durand and Yves Menu (Hôpital de Bicêtre) for their help in the CT scan examinations and to Xavier Maître for his assistance with the helium-3 polarization.

References

- [1] Callaghan PT. Principles of Nuclear Magnetic Resonance Microscopy. Oxford: Clarendon Press; 1991.
- [2] Callaghan PT, Coy A, MacGowan D, Packer KJ, Zelaya FO. Diffraction-like effects in NMR diffusion studies of fluids in porous solids. *Nature* 1991;351:467–9.
- [3] Song Y-Q, Ryu S, Sen PN. Determining multiple length scales in rocks. *Nature* 2000;406:178–81.
- [4] Brownstein KR, Tarr CE. Importance of classical diffusion in NMR studies of water in biological cells. *Phys Rev A* 1979;19:2446–53.
- [5] Kuchel PW, Coy A, Stilbs P. NMR “diffusion-diffraction” of water revealing alignment of erythrocytes in a magnetic field and their dimensions and membrane transport characteristics. *Magn Reson Med* 1997;37:637–43.
- [6] Moseley ME, Cohen Y, Mintorovitch J, Chileuit L, Shimizu H, Kucharczyk J, et al. Early detection of regional cerebral ischemia in cats: comparison of diffusion- and T2-weighted MRI and spectroscopy. *Magn Reson Med* 1990;14:330–46.
- [7] Le Bihan D. Looking into the functional architecture of the brain with diffusion MRI. *Nat Rev Neurosci* 2003;4:469–80.
- [8] Albert MS, Cates GD, Driehuis B, Happer W, Saam B, Springer CS, et al. Biological magnetic resonance imaging using laser-polarized 129Xe. *Nature* 1994;370:199–201.

- [9] Ebert M, Grossmann T, Heil W, Otten WE, Surkau R, Leduc M, et al. Nuclear magnetic resonance imaging with hyperpolarised helium-3. *Lancet* 1996;347:1297–9.
- [10] Saam BT, Yablonskiy DA, Kodibagkar VD, Leawoods JC, Gierada DS, Cooper JD, et al. MR imaging of diffusion of ^3He gas in healthy and diseased lungs. *Magn Reson Med* 2000;44:174–9.
- [11] Peces-Barba G, Ruiz-Cabello J, Cremillieux Y, Rodríguez I, Dupuich D, Callot V, et al. Helium-3 MRI diffusion coefficient: correlation to morphometry in a model of mild emphysema. *Eur Respir J* 2003;22:14–9.
- [12] The World Health Organization estimates that 2.74 million people died of COPD (chronic obstructive pulmonary diseases) worldwide in 2000.
- [13] Weibel ER. The Pathway for oxygen. Structure and function in the mammalian respiratory system. Cambridge (MA): Harvard University Press; 1984.
- [14] Sapoval B, Filoche M, Weibel E. Smaller is better-but not too small: A physical scale for the design of the mammalian pulmonary acinus. *Proc Natl Acad Sci U S A* 2002;99:10411–6.
- [15] Kitaoka H, Tamura S, Takaki R. A three-dimensional model of the human pulmonary acinus. *J Appl Physiol* 2000;88:2260–8.
- [16] American Thoracic Society. Standards for the diagnosis and care of patients with chronic obstructive pulmonary disease. *Am J Respir Crit Care Med* 1995;152:S77–S121.
- [17] Swift AJ, Wild JM, FICHELE S, Woodhouse N, Fleming S, Waterhouse J, et al. Emphysematous changes and normal variation in smokers and COPD patients using diffusion ^3He MRI. *Eur J Radiol* 2005;54:352–8.
- [18] Woods J-C, Choong CK, Yablonskiy DA, Bentley J, Wong J, Pierce JA, et al. Hyperpolarized ^3He diffusion MRI and histology in pulmonary emphysema. *Magn Res Med* 2006;56:1293–300.
- [19] Yablonskiy DA, Sukstanskii AL, Leawoods JC, Gierada DS, Bretthorst GL, Lefrak SS, et al. Quantitative in vivo assessment of lung microstructure at the alveolar level with hyperpolarized ^3He diffusion MRI. *Proc Natl Acad Sci U S A* 2002;99:3111–6.
- [20] FICHELE S, Paley MNJ, Woodhouse N, Griffiths PD, van Beek EJR, Wild JM. Finite-difference simulations of ^3He diffusion in 3D alveolar ducts: comparison with the “cylinder model”. *Magn Res Med* 2004;52:917–20.
- [21] Grebenkov DS, Guillot G, Sapoval B. Restricted diffusion in a model acinar labyrinth by NMR: theoretical and numerical results. *J Magn Reson* 2007;184:143–56.
- [22] Mata JF, Altes TA, Cai J, Ruppert K, Mitzner W, Hagspiel KD, et al. Evaluation of emphysema severity and progression in a rabbit model: comparison of hyperpolarized ^3He and ^{129}Xe diffusion MRI with lung morphometry. *J Appl Physiol* 2007;102:1273–80.
- [23] Kuethe DO, Caprihan A, Fukushima E, Waggoner RA. Imaging lungs using inert fluorinated gases. *Magn Reson Med* 1998;39:85–8.
- [24] Jacob RE, Chang YV, Choong CK, Bierhals A, Hu DZ, Zheng J, et al. ^{19}F MR imaging of ventilation and diffusion in excised lungs. *Magn Reson Med* 2005;54:577–85.
- [25] Stejskal EO, Tanner JE. Spin diffusion measurements : spin echoes in the presence of a time-dependent field gradient. *J Chem Phys* 1965;42: 288–92.
- [26] Mattiello J, Bassar PJ, LeBihan D. Analytical calculation of the b matrix in diffusion imaging. In: LeBihan D, editor. Diffusion and perfusion magnetic resonance imaging. New York: Raven Press; 1995. p. 77–90.
- [27] Caprihan A, Wang LZ, Fukushima E. A multiple-narrow-pulse approximation for restricted diffusion in a time-varying field gradient. *J Magn Reson A* 1996;118:94–102.
- [28] Callaghan PT. A simple matrix formalism for spin echo analysis of restricted diffusion under generalized gradient waveforms. *J Magn Reson* 1997;129:74–84.
- [29] Barzykin AV. Theory of spin echo in restricted geometries under a step-wise gradient pulse sequence. *J Magn Reson* 1999;139: 342–353.
- [30] Axelrod S, Sen PN. Nuclear magnetic resonance spin echoes for restricted diffusion in an inhomogeneous field: methods and asymptotic regimes. *J Chem Phys* 2001;114:6878–95.
- [31] Grebenkov DS. NMR survey of reflected Brownian motion. *Rev Mod Phys* 2007;79:1077–137.
- [32] Mitra PP, Sen PN, Schwartz LM, Le Doussal P. Diffusion propagator as a probe of the structure of porous media. *Phys Rev Lett* 1992;68:3555–8.
- [33] Mitra PP, Sen PN, Schwartz LM. Short-time behavior of the diffusion coefficient as a geometrical probe of porous media. *Phys Rev B* 1993;47:8565–74.
- [34] de Swiet TM, Sen PN. Decay of nuclear magnetization by bounded diffusion in a constant field gradient. *J Chem Phys* 1994;100: 5597–604.
- [35] Hürlimann MD, Helmer KG, Latour LL, Sotak CH. Restricted diffusion in sedimentary rocks. Determination of surface-area-to-volume ratio and surface relaxivity. *J Magn Reson A* 1994;111:169–78.
- [36] Helmer KG, Hürlimann MD, de Swiet TM, Sen PN, Sotak CH. Determination of ratio of surface area to pore volume from restricted diffusion in a constant field gradient. *J Magn Reson A* 1995;115:257–9.
- [37] Mair RW, Wong GP, Hoffmann D, Hürlimann MD, Patz S, Schwartz LM, et al. Probing porous media with gas diffusion NMR. *Phys Rev Lett* 1999;83:3324–7.
- [38] Choukeife J, Maître X, Tastevin G, Nacher P-J. On-site production of hyperpolarized ^3He for lung MRI. *Proc Int Soc Magn Res Med* 2003;11:1391.
- [39] Nacher P-J, Tastevin G, Maître X, Dollat X, Lemaire B, Olejnik J. A peristaltic compressor for hyperpolarized helium. *Eur Radiol* 1999;9:B18.
- [40] Bidinosti CP, Choukeife J, Nacher P-J, Tastevin G. In vivo NMR of hyperpolarized ^3He in the human lung at very low magnetic fields. *J Magn Reson* 2003;162:122–32.
- [41] Grebenkov D. http://pmc.polytechnique.fr/pagesperso/dg/MCF/MCF_e.htm.
- [42] Grebenkov DS, Guillot G. Numerical MRI of the translational diffusion in branching three-dimensional labyrinths of a model pulmonary acinus. *MAGMA* 2005;18:S128.
- [43] Maître X, Habib D, de Rochefort L, Fournier A, Bernigaud V, Senaj V, et al. Gradient calibration for gas ADC mapping. *Proc ESMRMB MAGMA* 2005;18:S147.
- [44] Wang C, Miller GW, Altes TA, de Lange E, Cates GD, Mugler JP. Time dependence of ^3He diffusion in the human lung: Measurement in the long-time regime using stimulated echoes. *Magn Reson Med* 2006;56: 296–309.
- [45] Habib D, Perez-Rial S, Pérez-Sánchez JM, Rodríguez I, Ruiz-Cabello J, Guillot G. In vivo diffusion measurements of hyperpolarized helium-3 in rat lungs at low field: time dependence with a fast sequence. *Proc Int Soc Magn Reson Med* 2007;14:457.
- [46] Woods JC, Yablonskiy DA, Choong CK, Chino K, Pierce JA, Hogg JC, et al. Long-range diffusion of hyperpolarized ^3He in explanted normal and emphysematous human lungs via magnetization tagging. *J Appl Physiol* 2005;99:1992–7.